Attosecond wave-packet interferometry using two-color XUV pulses

D. M. Villeneuve [1] and Hiromichi Niikura [2,*]

[1]*Joint Attosecond Science Laboratory, National Research Council of Canada and University of Ottawa,*
100 Sussex Drive, Ottawa, Ontario, Canada K1A 0R6
[2]*Department of Applied Physics, Waseda University, 3-4-1 Okubo, Shinjuku, Tokyo 169-8555, Japan*

We generate two attosecond pulse trains (XUV_ω and $XUV_{2\omega}$) by focusing an infrared (IR, ω) laser pulse and its temporally advanced second harmonic field (2ω) into an argon gas jet. Using the two XUV pulses and another infrared pulse, we perform two types of experiments for electron wave-packet interferences with attosecond time resolution. The delays between three pulses, $XUV_{2\omega}$, XUV_ω, and IR, are independently controlled. First, at a fixed delay between the $XUV_{2\omega}$ and the IR pulses, we record the velocity map images of photoelectrons ionized from helium as a function the two XUV pulses. The photoelectron signal intensity is modulated with the period corresponding to the energy separation between the $1s$ and $4p$ states of helium, 174 as. This indicates that the $4p$ Rydberg state is populated by harmonic 15 (15ω) in both $XUV_{2\omega}$ and XUV_ω pulses. Second, we overlap $XUV_{2\omega}$ with the IR pulse in time and record the VMI images as a function of the two pulses. By analyzing the interference pattern in the VMI images, we find that harmonic 13 (13ω) from $XUV_{2\omega}$ is responsible for the generation of the g wave in the ionization continuum. Our method of using two XUV pulses containing different sets of harmonics can simplify attosecond XUV interferometry experiments.

I. INTRODUCTION

An attosecond laser pulse (XUV) or high-order harmonic generation (HHG) enables one to access the quantum nature of an electron wave function. The relative phase or photoionization delay can be retrieved by using interference between the multiphoton ionization process caused by the XUV combined with an infrared (IR, ω) pulse [1–5]. A complete characterization of the angular momentum components in the photoelectron wave function has been demonstrated [4–5]. Other method to measure the relative phase is to employ two XUV pulses with the same photon energy [6–10]. The electron wave function populated by one XUV pulse interferes with that produced by the other wave packet. By changing the delay between the two XUV pulses, the interference pattern is modulated, from which the relative phase of the wave function is obtained. In these wave-packet interferometry experiments [6–10], two identical XUV pulses generated from the IR field were utilized.

In this study, we demonstrate wave-packet interferometry by using two XUV pulses consisting of a different set of harmonics. The XUV pulses are attosecond pulse trains whose spectra are composed of odd harmonics of the driving field. The XUV pulses are generated by focusing the second harmonic (2ω, 392 nm) and the delayed infrared (ω, 784 nm) fundamental pulses into an argon gas jet. One XUV pulse contains the odd harmonics of the ω (IR) field, referred to as XUV_ω, and the other, referred to as $XUV_{2\omega}$, contains mostly the odd harmonics of the 2ω. The delay between the two XUVs is controlled with attosecond time resolution, thanks to

the inline pulse generation scheme. The pair of XUV pulses with the IR pulse then photoionize helium atoms in a second gas jet in a velocity map imaging electron spectrometer (VMI).

Figure 1(a) shows the energy levels of helium. The harmonic 15ω resonantly populates the $4p$ Rydberg state from the $1s$ ground state. From the $4p$ state, an additional IR photon produces s and d waves in the ionization continuum. Figure 1(b) illustrates the interference scheme performed by two XUV pulses. The population produced in the $4p$ Rydberg state by $XUV_{2\omega}$ interferes with that produced by the delayed XUV_ω pulse. The velocity map images of photoelectrons produced from the $4p$ state with one IR photon ionization are recorded as a function of the two delays. In the first interference experiment, we fix the delay between the $XUV_{2\omega}$ pulse and the IR pulse, $T_{\text{XUV-IR}}$, and change the delay between the $XUV_{2\omega}$ pulse and the XUV_ω pulse, τ. We observe the intensity modulation in the VMI as a function of τ, which indicates that 15ω is included in both XUV_ω and $XUV_{2\omega}$. In the second interference experiment, we employ the multiphoton ionization process with the $XUV_{2\omega}$ pulse and the IR pulse when both pulses are temporally overlapped. By analyzing the VMIs recorded as a function of the $T_{\text{XUV-IR}}$, we show that $XUV_{2\omega}$ produces a g-wave photoelectron originating from 13ω in $XUV_{2\omega}$.

II. EXPERIMENTAL SETUP

Figure 2 illustrates the optical setup for the experiments. The experimental setup is similar to that used in previous experiments [4–5], except for a modification of the delay optics placed before the high-order harmonic generation chamber. A 1-kHz, 35-fs, ~784-nm laser pulse (ω) is generated from
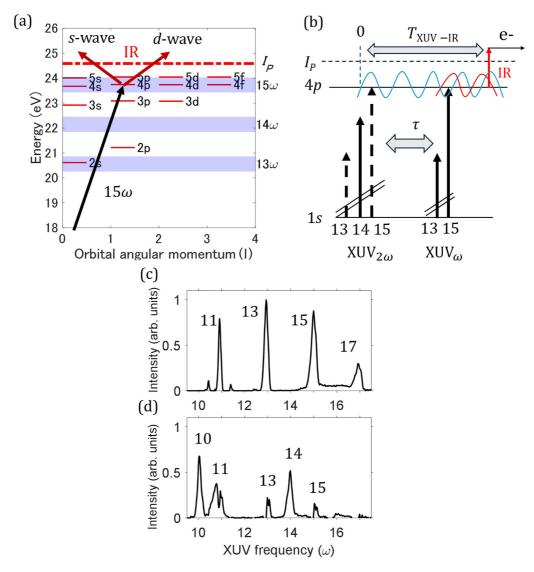
---

*Contact author: niikura@waseda.jp

FIG. 1. (a) The energy diagram of helium and two-photon ionization pathways. The blue shaded areas show the location of the high-order harmonics. (b) Interference scheme using $XUV_{2\omega}$ and XUV_ω. The wave packets produced in the $4p$ Rydberg state are probed with one photon ionization by the IR pulse. The time delay τ between $XUV_{2\omega}$ and XUV_ω is adjustable, as is the time delay $T_{XUV\text{-}IR}$ between $XUV_{2\omega}$ and IR. (c) High-order harmonic spectrum of XUV_ω with the ω driving pulse alone. (d) High-order harmonic spectrum of $XUV_{2\omega}$, which contains some residual odd harmonics of XUV_ω.

a dual-stage Ti:sapphire amplifier system (Komodo-Dragon, KMlabs). A half-moon-shaped fused silica plate (FS1) splits the pulse into the upper and lower parts, labeled as beams A and B. Both beams are transmitted to a β-barium borate (β-BBO) crystal to generate the second-order harmonic field, 2ω. We adjust the delay between the ω and 2ω using a fused silica plate (FS) and a calcite plate. By rotating the fused silica plate, we control the delay τ. A dual wave plate makes both polarizations parallel to each other. Both beams are focused into an argon gas jet to produce the XUV_ω and $XUV_{2\omega}$ attosecond pulse trains. The harmonics produced by beam A are reflected on the two silicon mirrors, eliminating the ω and 2ω fields. Meanwhile, beam B is reflected on the aluminum-coated part of the mirrors. Both beams are refocused by a gold-coated toroidal mirror into the ionization region in the VMI apparatus. Another half-moon-shaped fused silica plate (FS2) is inserted in beam B, which blocks the XUV pulses in

the beam, giving the ω dressing field. The delay of the ω beam B is controlled by rotating FS1. We could find no evidence that the 2ω field in beam B contributes to the photoionization.

Both XUV pulses and the IR dressing field are focused into the helium gas jet in the VMI. Photoelectron momenta are mapped onto the MCP detector. The polarization direction of all three pulses lies in the plane of the MCP. The polarization axis lies along the vertical axis in the VMI images, which defines the polar axis in the spherical coordinate system. The XUV pulses pass into a XUV spectrometer to record the spectra of the XUV pulses. By detuning the BBO crystal that produced the $XUV_{2\omega}$ pulse, it was possible to record the spectrum of XUV_ω alone [Fig. 1(c)]. However, the spectrum of $XUV_{2\omega}$ was in the presence of XUV_ω, so that the spectrum of $XUV_{2\omega}$ was inferred by subtracting the two spectra [Fig. 1(d)]. To do this, we normalize the intensity of 17ω in both spectra. In addition to 10ω and 14ω, $XUV_{2\omega}$ contains
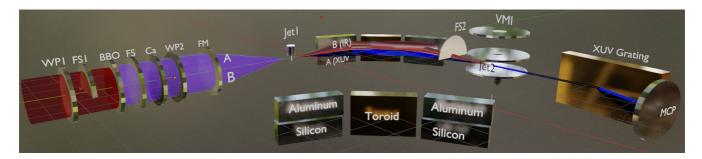
FIG. 2. Illustration of the optical setup. The 784-nm beam from the Ti:sapphire laser enters from the left. A wave plate (WP1) adjusts the polarization to vertical. A half-moon-shaped fused silica plate (FS1) delays the top half of the beam, labeled A. A BBO crystal generates 392 nm by second-order harmonic generation. A fused silica plate (FS) and a calcite plate (Ca) control the delay between the 784-nm (ω) and 392-nm (2ω) pulses. A dual-wavelength wave plate (WP2) makes the two polarizations horizontal. The two collinear pulses are then focused into the vacuum chamber by a spherical focusing mirror (FM) (shown as a lens for clarity). Both pulses, separated in time, produce attosecond pulse trains in the argon gas jet (Jet1), leading to high-order harmonics. The two half-beams, A and B, are reflected off two mirrors with split coatings and a toroidal mirror. Beam B then passes through a half-moon fused silica plate (FS2) that removes the XUV from beam B, leaving primarily 784 nm that is used as the dressing field. Meanwhile, Beam A has 784 nm removed from it by the silicon-coated mirrors, producing attosecond pulse trains $XUV_{2\omega}$ and XUV_{ω}. All three pulses are focused into a second gas jet (Jet2) containing helium gas, inside a velocity map imaging (VMI) spectrometer. Photoelectrons are accelerated upwards to the microchannel plate (MCP) which records the electron momentum as a function of delay. The unused HHG beams enter a flat-field XUV spectrometer which records the HHG spectrum.

additional weak harmonics due to the coupling of the 2ω field with a much weaker ω field from the tail of the main 784-nm pulse.

III. RESULTS AND DISCUSSIONS

A. The XUV-IR delay dependence

Figure 3 shows the photoelectron kinetic energy distributions as a function of the XUV-IR delay ($T_{\text{XUV-IR}}$) for two cases: in the presence of (a) both ω and 2ω fields and (b) only the ω field. The photoelectrons ejected parallel to the polarization axis of the laser pulses are selected. Figure 4 shows the VMI images at selected $T_{\text{XUV-IR}}$ delays, labeled as A–E in Fig. 3. Several peaks are observed and labeled. The peaks labeled as $3p$ and $4p$ are identified as the photoelectrons produced from $3p$ and $4p$ Rydberg states plus one IR photon [11]. The peaks labeled as 17ω and 19ω are the photoelectrons produced by direct ionizations due to 17ω and 19ω. Since these two peaks are produced by the XUV_{ω} pulse alone, they are observed regardless of the XUV-IR delay.

In delay range A, only the peaks due to 17ω and 19ω are recognized in both Figs. 3(a) and 3(b). In delay range B, a sixfold angular distribution is observed in B of Fig. 4(a) in the lower kinetic energy region, while no corresponding peak is recognized in Fig. 4(b). The photoelectron signal observed in Fig. 4(a) remains for $T_{\text{XUV-IR}} > 0$, though the angular distribution changes from that in region B. From these observations, we identify that the $XUV_{2\omega}$ is temporally overlapped with the IR pulse in delay range B, where we define the delay $T_{\text{XUV-IR}}$ to be zero. In Sec. III C, we investigate the photoionization process observed in $T_{\text{XUV-IR}} = 0$ in detail.

In delay range D, the intensity of the peaks labeled as $3p$ and $4p$ is enhanced, and another peak appears in between the 17ω and 19ω peaks. The peak is identified as a RABBIT sideband produced by continuum coupling of the IR field with the 17ω and 19ω photoelectrons [3]. From this observation, we identify that XUV_{ω} is temporally overlapped with the IR pulse in delay range D, $T_{\text{XUV-IR}} \sim 100$ fs. In the range

$T_{\text{XUV-IR}} > 100$ fs, the photoelectron peaks produced from the $3p$ and $4p$ states remain while the sideband disappears. We note that no photoelectron signals due to 16ω and 18ω are
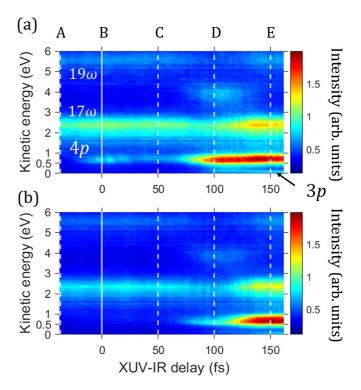

FIG. 3. The photoelectron signal intensity as a function of the XUV-IR delay when the high-order harmonics are generated by (a) both ω and 2ω fields and (b) only the ω field. Photoelectrons emitted parallel to the polarization axis of the laser pulse are selected. We define time zero as when the $XUV_{2\omega}$ and the IR pulses are overlapped in time. Photoelectrons produced by direct one-photon ionization by 17ω and 19ω are seen at all delay times, whereas two-photon processes are limited to when the pulses overlap.
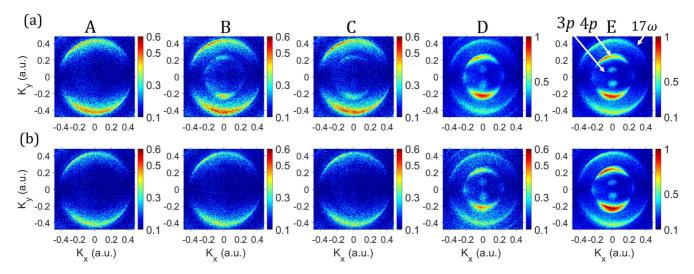
FIG. 4. The velocity map images recorded at the XUV-IR delays labeled as A–E in Fig. 3. Panels (a) and (b) correspond to the conditions of panels (a) and (b) in Fig. 3, i.e., both $XUV_{2\omega}$ and XUV_ω in panel (a) and only using XUV_ω in panel (b). The polarization axis of all three pulses lies in the vertical direction in these images. The color bar indicates the relative intensity of the photoelectron yields (arbitrary units). With both $XUV_{2\omega}$ and XUV_ω being used in panel (a), photoelectrons are produced by residual 15ω from $XUV_{2\omega}$ plus one ω photon after time zero at time B. At time D, 15ω from XUV_ω plus one ω photon adds to the $4p$ channel, as well as to some $3p$ channels.

observed in delay range A, indicating that $XUV_{2\omega}$ does not contain these two harmonics.

B. The XUV_ω-$XUV_{2\omega}$ delay dependence

Next, we fix $T_{XUV\text{-}IR} = 161$ fs and record the XUV_ω and $XUV_{2\omega}$ delay dependence of the VMI photoelectron spectra. Figure 5(a) plots the high-order harmonic spectrum as a function of the ω-2ω delay. 12ω and 16ω are suppressed compared to other harmonics, ensuring that direct photoionization due to 16ω does not interfere with the 15ω plus one IR photon ionization process.

Figure 5(b) plots the photoelectron signal intensity as a function of the delay between the ω and 2ω fields. The photoelectrons ejected parallel to the polarization axis of the laser pulses are selected. The intensity of photoelectrons produced through the $4p$ Rydberg state is modulated, and the lineout of the averaged signals emitted in the upwards and downwards directions is plotted in Fig. 5(c). The intensity variation of the spectrum of 15ω is also plotted, showing that there is no modulation in the HHG spectrum.

As has been mentioned in the previous section, the ω-2ω delay is changed by rotating the 1.1-mm fused silica plate FS to increase the relative optical path length of the ω and 2ω fields due to the different phase delays. The modulation period corresponding to the energy separation between the $1s$ and $4p$ Rydberg states ($\Delta E = 23.742$ eV) is 174 as. The calculated delay based on the phase delays of ω and 2ω by a tilted plate differs by 5.5% from this value, corresponding to a 0.06-mm thickness error of the fused silica plate. Since the energy level of the $4p$ state is well defined [11], we use the observed modulation period for the calibration of the delay time axis.

In order to see what photoelectron features are associated with the $4p$ state, we model the photoelectron intensity as a function of the ω-2ω delay τ by $I = |\psi_1 + \psi_2 \exp(i\omega_{4p}\tau)|^2$, where $\omega_{4p} = \Delta E/\hbar$ and ψ_1 and ψ_2 are the wave functions

produced by XUV_ω and $XUV_{2\omega}$. We fit the signal intensity modulation at each momentum (k_x, k_y) of the VMI images at all time delays τ using the equation

$$I(k_x, k_y; \tau) = A(k_x, k_y)\cos[\omega_{4p}\tau + B(k_x, k_y)] + C(k_x, k_y),$$

(1)

where $A(k_x, k_y)$, $B(k_x, k_y)$, and $C(k_x, k_y)$ are the distributions obtained by fitting to the experimental data. Each pixel is fit independently to this model. The results of fitting are shown in Fig. 6 for (a) amplitude A, (b) phase B, and (c) the DC-component C at each pixel. In Fig. 6(d), the phase and amplitude distributions are plotted together using an *hsv* two-dimensional color map [5]. The distribution of the DC component is mostly consistent with the distributions shown in the VMI images. In the amplitude and the phase distributions, the intensity of the photoelectron signal ionized from the $4p$ state and the peak labeled as α are recognized. Note that the $3p$ feature does not appear in the amplitude function, demonstrating that this feature is not associated with the $4p$ state.

The peak α has the same electron energy as the direct ionization of 17ω. Since we fit the photoelectron intensity modulated with the $1s$–$4p$ transition frequency, the photoelectron signal due to direct ionization of 17ω is excluded. The peak α is produced by two-photon IR absorption from the $4p$ state. The phase of the peak labeled as α is identical with that of the peaks from $4p$.

We now look at the photoelectron angular distributions for the peaks labeled as $4p$ and α. By using a polar coordinate, we define an angular function Ψ as $\Psi(r, \theta) = A(r, \theta)\exp[iB(r, \theta) + i\beta(r)]$ with the momentum radius r in which the peaks of $4p$ and α are observed. Here β is the angle-independent arbitrary phase, selected so that the amplitude of the imaginary part is minimized. With the above-mentioned definition, $\Psi(r, \theta)$ is the product of the wave functions, $\Psi(r, \theta) = \psi_1(r, \theta)\psi_2^*(r, \theta)\exp[i\beta(r)]$ [5]. The
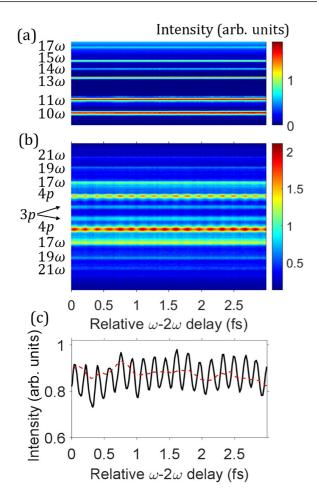
FIG. 5. (a) The high-order harmonic spectra as a function of the relative ω-2ω delay, τ. (b) The intensity of the photoelectron signals emitted parallel to the polarization direction of the laser pulse as a function of the same delay. The photoelectron signal produced by the direct ionization due to the $n\omega$ harmonic and those associated with the $3p$ and $4p$ states are labeled. (c) The intensity modulation of the photoelectrons produced through the $4p$ state as a function of the delay (solid line). The signal intensities of photoelectrons emitted in both upwards and downwards directions are averaged. The spectral intensity of 15ω is plotted as a dotted line. The clear modulation of the photoelectron signal is at the frequency of the helium $1s$–$4p$ transition.

terms $\psi_{1,2}(r, \theta)$ are the sum of the angular momentum components, $\psi_{1,2}(r, \theta) = a^s_{1,2}(r)Y_{0,0}(\theta) + a^d_{1,2}(r)Y_{2,0}(\theta)$ for the peak labeled as $4p$, and $\psi_{1,2}(r, \theta) = a^p_{1,2}(r)Y_{1,0}(\theta) + a^f_{1,2}(r)Y_{3,0}(\theta)$ for the peak labeled as α. Here $a^i_{1,2}$ are the complex amplitudes for the s, p, d, and f waves, and $Y_{\ell,0}$ are the spherical harmonics with $m_\ell = 0$. Note that only $m_\ell = 0$ states can be populated using linearly polarized light starting from the $1s$ state of He.

Figures 6(e) and 6(f) plot the real and imaginary parts of Ψ for two peaks. The angular distributions of the real part are consistent with the features of d and f waves for the ring $4p$ and α, while the angular distribution of the imaginary part is almost independent of the angle. In contrast to the interference of wave functions with two opposite parities [4–5], in the present case it is difficult to determine the complex amplitudes
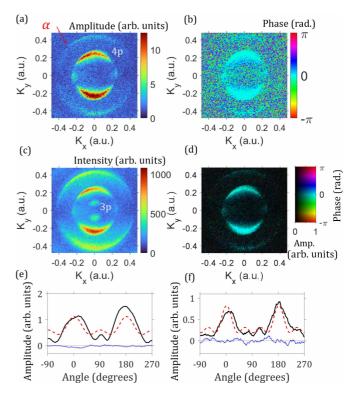

FIG. 6. (a) The fitted amplitude, (b) phase, and (c) DC distributions of the photoelectron as a function of the ω-2ω delay, τ. (d) Both amplitude and phase distributions are displayed together using an *hsv* color map, where the amplitude and phase are represented by brightness and color. The amplitude and phase images show those photoelectron features that are associated with the $1s$–$4p$ transition frequency. (e), (f) The angular distribution of the photoelectron signal labeled as $4p$ (e) and α (f) in panel (a). Black and blue solid lines are the real and imaginary parts of Ψ. The red dotted lines are the calculated angular distributions of the square of the d and f waves. The polarization axis of all three pulses lies in the vertical direction in the VMI images, i.e., $k_x = 0$. The $\theta = 0$ axis in the polar coordinate system is at the 12 o'clock position in the VMI images.

$a^i_{1,2}$ for all components. Thus, we make the assumption that the wave functions ψ_1 and ψ_2 have the same amplitude, and we plot the calculated angular distribution of the square of the d and f waves in the same figures. The calculated lines are comparable with the observed ones (solid line). This indicates that from the $4p$ Rydberg state, the d wave is dominantly produced in the ionization continuum, and from the d wave, the f wave is dominantly produced by the absorption of one additional IR photon.

C. Interference with the XUV$_{2\omega}$ and the IR pulse

Next, we record the VMI as a function of the XUV-IR delay, $T_{\text{XUV-IR}}$, when the XUV$_{2\omega}$ and IR pulses are temporally overlapped. Figure 7(a) plots the intensity distribution of photoelectrons emitted parallel to the polarization axis as a function of $T_{\text{XUV-IR}}$. The photoelectron intensity is modulated with approximately the period of the IR pulse. The photoelectrons emitted in the upward direction have an opposite modulation phase compared with those emitted in the downward direction.
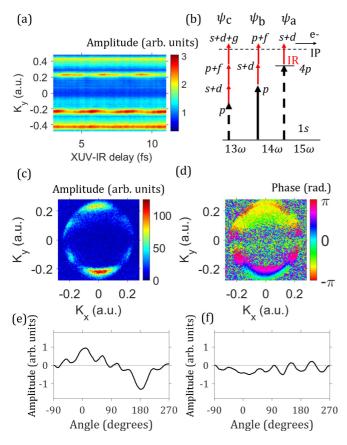
FIG. 7. (a) The signal intensity of photoelectrons ejected parallel to the laser polarization axis as a function of T_{XUV-IR} in the region where $XUV_{2\omega}$ and IR pulses overlap in time. (b) The multiphoton ionization pathways. (c) The fitted amplitude $A_1(k_x, k_y)$. (d) The fitted phase $B_1(k_x, k_y)$. Panels (e) and (f) show the real and imaginary parts, respectively, of the angular distribution of Ψ_1 at the momentum radius around 0.23 (a.u.). We adjust the arbitrary phase so that the intensity of the imaginary part is minimized.

The modulation of the photoelectron intensity indicates that $XUV_{2\omega}$ allows several multiphoton ionization pathways. The interference of wave packets in the ionization continuum can occur between the three multiphoton ionization pathways, 15ω plus one IR photon ($15\omega + IR$), 14ω plus two IR photons ($14\omega + 2IR$), and 13ω plus three photons ($15\omega + 3IR$) [Fig. 7(b)]. Note that the intensity of harmonic 12ω is suppressed as is seen in Fig. 1. Each pathway produces an electron wave function labeled as Ψ_a, Ψ_b, or Ψ_c. The angular momentum components consisting of these wave functions are depicted in the figure. To elucidate what angular momentum components are included in the photoelectron wave packet, we fit the photoelectron intensity curve as a function of T_{XUV-IR} at each momentum of the VMI images using the equation

$$
\begin{aligned}
&I_{2\omega}(k_x, k_y; T_{XUV-IR}) \\
&= A_1(k_x, k_y)\cos[\omega T + B_1(k_x, k_y)] \\
&\quad + A_2(k_x, k_y)\cos[2\omega T + B_2(k_x, k_y)] + C(k_x, k_y),
\end{aligned}
\tag{2}
$$

where $A_{1,2}$ and $B_{1,2}$ are the amplitude and phase distributions modulated with the angular frequency of ω and 2ω, and C is the DC component.

Figures 7(c) and 7(d) show the fitted amplitude A_1 and phase B_1 distributions. The other fitted distributions are shown in Fig. 8 in Appendix A. The amplitude of A_1 is approximately ten times larger than A_2 and thus the component modulated with ω is dominant over that with 2ω. The angular distribution of the amplitude, A_1, exhibits the sixfold structure, while the angular distribution of the phase, B_1, shows a more complicated structure.

From A_1 and B_1, we generate an angular distribution $\Psi_1(r, \theta) = A_1(r, \theta)\exp[iB_1(r, \theta) + i\beta_1(r)]$, where r is the momentum radius around 0.23 a.u. and β_1 is an arbitrary phase. In the three-path interference, $\Psi_1(\theta; r)$ is a sum of the product of the wave functions produced with two adjacent ionization pathways, $\Psi_1(r, \theta) = \psi_a\psi_b^* + \psi_b\psi_c^*$ [5]. Each wave function is a coherent sum of the partial wave components $\psi_i(r, \theta) = \sum a_\ell^i Y_{\ell,0}$, where a_ℓ^i is the complex amplitude. In the case of the three-path interference, disentangling Ψ_1 into the wave function for each pathway is difficult. However, from the measured angular distributions of Ψ_1, one can obtain information about which angular momentum components contribute to the ionization process.

Figures 7(e) and 7(f) show the real and imaginary parts of Ψ_1 as a function of angle. Here we select the arbitrary phase β_1 so that the imaginary part is minimized. In Fig. 7(e), the angular distribution has seven peaks, indicating that Ψ_1 includes f and g waves. The number of peaks in the angular momentum distribution is given by $\ell + \ell'$, where ℓ and ℓ' are the angular momentum quantum numbers of the partial waves. In Appendix B, we plot the $Y_{\ell,0}Y_{\ell',0}$ for several combinations of the angular momentum components. The g wave is produced in the pathway ψ_c with 13ω plus three IR photon ionization. The appearance of the g-wave component through this pathway has been noted elsewhere [11].

IV. CONCLUSION

We have demonstrated wave-packet interferometry in the XUV region using two attosecond pulse trains produced by temporally separated ω and 2ω fields. Thanks to the additional harmonics included in $XUV_{2\omega}$, the electron wave packet produced in the $4p$ Rydberg state of helium interferes with that produced by XUV_ω. In other experiments [6–10], noncollinear interferometers were used to control the delay between pulses; in our experiment, an all-collinear optical arrangement was used, providing stability on the few-attosecond timescale. Our method can be applied to attosecond XUV interferometry with other atoms and molecules.

We have shown that additional harmonics are produced with the odd harmonics of the 2ω field, i.e., $14\omega \pm 1\omega$. When overlapping the ω and 2ω fields in time and focusing them into the gas jet, both odd and even harmonics are generated [12–14]. In our case, the ω and 2ω fields are separated by $\sim$100 fs, which is approximately three times larger than the laser pulse duration. One possible explanation for the appearance of the additional harmonics in the $XUV_{2\omega}$ spectrum is due to a weak field from the tail of the ω pulse perturbing the 2ω field, leading to field mixing. Our experimental result will
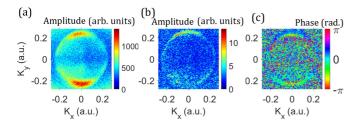
FIG. 8. (a) The fitted DC component $C(k_x, k_y)$, (b) amplitude $A_2(k_x, k_y)$, and (c) phase $B_2(k_x, k_y)$ to the $A_2(k_x, k_y)\cos[2\omega T + B_2(k_x, k_y)]$ term.

stimulate theoretical studies for the generation mechanism of the attosecond pulse train with additional harmonics.

ACKNOWLEDGMENTS

DATA AVAILABILITY

The data that support the findings of this article are not publicly available upon publication because it is not technically feasible and/or the cost of preparing, depositing, and hosting the data would be prohibitive within the terms of this research project. The data are available from the authors upon reasonable request.

APPENDIX A: OTHER FITTED DISTRIBUTIONS

Figure 8 shows the fitted distributions for (a) DC distribution $C(k_x, k_y)$, the amplitude $A_2(k_x, k_y)$, and the
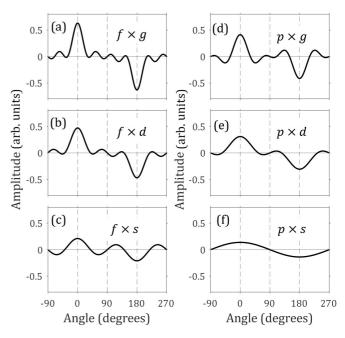

FIG. 9. The calculated angular distributions $Y_{\ell,0}Y_{\ell',0}$ for the g ($\ell = 4$), f ($\ell = 3$), d ($\ell = 2$), p ($\ell = 1$), and s ($\ell = 0$) partial waves.

phase $B_2(k_x, k_y)$ distributions for the 2ω component in Eq. (2).

APPENDIX B: THE CALCULATED ANGULAR DISTRIBUTIONS FOR THE PRODUCTS OF SPHERICAL HARMONICS

In Fig. 9, we plot the calculated angular distributions of $Y_{\ell,0}Y_{\ell',0}$ for ℓ and $\ell' = 4$, 3, 2, 1, and 0, corresponding the g, f, d, p, and s waves. The number of peaks is consistent with $\ell + \ell'$. From the number of modulations, the angular momentum components included in the ionization pathways can be identified.

[1] F. Krausz and M. Ivanov, Rev. Mod. Phys. **81**, 163 (2009).

[2] J. M. Dahlström, A. L'Huillier, and A. Maquet, J. Phys. B: At. Mol. Opt. Phys. **45**, 183001 (2012).

[3] Y. Mairesse, A. de Bohan, L. J. Frasinski, H. Merdji, L. C. Dinu, P. Monchicour, P. Breger, P. Kovačev, R. Taïeb, B. Carré, H. G. Muller, P. Agostini, and P. Salières, Science **302**, 1540 (2003).

[4] D. M. Villeneuve, P. Hockett, M. J. J. Vrakking, and H. Niikura, Science **356**, 1150 (2017).

[5] T. Nakajima, T. Shinoda, D. M. Villeneuve, and H. Niikura, Phys. Rev. A **106**, 063513 (2022).

[6] C. Corsi, A. Pirri, E. Sali, A. Tortora, and M. Bellini, Phys. Rev. Lett. **97**, 023901 (2006).

[7] J. B. Bertrand, H. J. Wörner, P. Salières, D. M. Villeneuve, and P. B. Corkum, Nat. Phys. **9**, 174 (2009).

[8] D. Azoury, O. Kneller, S. Rozen, B. D. Bruner, A. Clergerie, Y. Mairesse, B. Fabre, B. Pons, N. Dudovich, and M. Kruger, Nat. Photon. **13**, 54 (2019).

[9] M. H. Mustary, L. Xu, W. Wu, N. Haram, D. E. Laban, H. Xu, F. He, R. T. Sang, and I. V. Litvinyuk, Ultrafast Sci. **2022**, 9834102 (2022).

[10] O. Kneller, C. Mor, N. D. Klimkin, N. Yaffe, M. Krüger, D. Azoury, A. J. Uzan-Narovlansky, Y. Federman, D. Rajak, B. D. Bruner, O. Smirnova, S. Patchkovskii, Y. Mairesse, M. Ivanov, and N. Dudovich, Nat. Photon. **19**, 134 (2025).

[11] N. Mayer, P. Peng, D. M. Villeneuve, S. Patchkovskii1, M. Ivanov, O. Kornilov, M. J. J. Vrakking, and H. Niikura, J. Phys. B: At. Mol. Opt. Phys. **53**, 164003 (2020).

[12] T. Zuo, A. D. Bandrauk, M. Ivanov, and P. B. Corkum, Phys. Rev. A **51**, 3991 (1995).

[13] N. Dudovich, O. Smirnova, J. Levesque, Y. Mairesse, M. Yu. Ivanov, D. M. Villeneuve, and P. B. Corkum, Nat. Phys. **2**, 781 (2006).

[14] K. T. Kim, C. Zang, A. D. Shiner, B. E. Schmidt, F. Lègarè, D. M. Villeneuve, and P. B. Corkum, Nat. Photon. **7**, 958 (2013).